ACS OMEGA

Article

Cite This: ACS Omega 2018, 3, 9888−9898

http://pubs.acs.org/journal/acsodf

Nitrogen-Doped Nanoporous Carbon Nanospheroids for Selective Dye Adsorption and Pb(II) Ion Removal from Waste Water

Sukanya Kundu, Ipsita Hazra Chowdhury, and Milan Kanti Naskar*

Sol−Gel Division, CSIR-Central Glass & Ceramic Research Institute, Kolkata 700 032, India

Supporting Information

ABSTRACT: In the presence of melamine and block copolymers, namely, F108, F127, and P123, nitrogen-doped nanoporous carbon nanospheroids (N@CNSs) were synthesized by the hydrothermal process. The F127-modified sample (CNF127) exhibits the maximum Brunauer−Emmett−Teller (BET) surface area of 773.4 m^2/g with a pore volume of 0.877 cm^3/g. The microstructural study reveals that nanospheroids of size 50−200 nm were aggregated together to form a chainlike structure for all triblock copolymer-modified samples. The X-ray photoelectron spectroscopy study shows the binding energies of 398.33 and 400.7 eV attributed to sp^2 (C−N=C)- and sp^3 (C−N)-hybridized nitrogen-bonded carbons, respectively. The synthesized N@CNS samples showed selective adsorption of organic dye methylene blue (MB) in the presence of methyl orange (MO) as well as Pb(II) ion removal from contaminated water. The adsorptions for MB and Pb(II) ions followed pseudo-first-order and pseudo-second-order kinetic models, respectively. The sample CNF127 showed the highest adsorption of 73 and 99.82 mg/g for MB and Pb(II) adsorptions, respectively. The adsorption capacity for MB of the copolymer-modified samples follows the order CNF127 > CNP123 > CNF108, which corroborated with the mesoporosity as well as nitrogen content of the corresponding samples. The maximum % adsorption of Pb(II) follows the order CNF127 (99.82%) > CNF108 (98.74%) > CNP123 (91.82%), and this trend is attributed to the BET surface area of the corresponding samples. This study demonstrates multicomponent removal of water pollutants, both organic dyes and inorganic toxic metal ions.

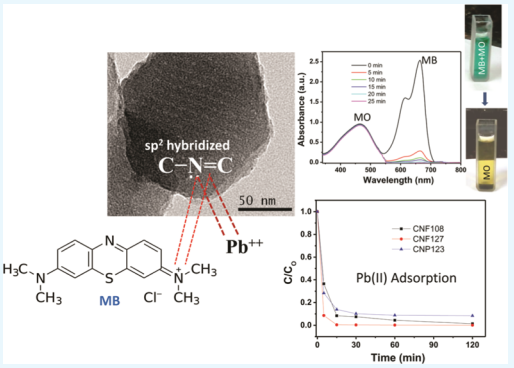

INTRODUCTION

With rapid industrial growth, water contamination by organic and inorganic pollutants has become an important environmental concern to living beings. Organic dyes are essential chemicals for a variety of industries like textile, pulp and paper, paints, cosmetics, pharmaceuticals, etc. The organic dyes are one of the major water pollutants causing carcinogenic and teratogenic effects on human beings.[1] There are various methods like ozone treatment, photocatalysis, adsorption, ion exchange, electrochemical oxidation, etc. for the removal of organic dyes. Among the different methods, adsorption is the most effective method for dye degradation because of total removal of the dye content without formation of any by-products.[2] Among the inorganic pollutants, lead is found to be a dreadful water pollutant causing detrimental effects on human body like anemia, encephalopathy, hepatitis, nephritic syndrome, etc.[3] Various industries like battery and chemical manufacturing, petrochemicals, agrochemicals, etc. are the main sources of Pb poisoning in waste water. Different processes like precipitation, oxidation, ion exchange, filtration, reverse osmosis, electrodialysis, adsorption, etc. are reported for the removal of lead ions from contaminated water. Among the various processes, adsorption is the promising process because of its high efficiency; effectiveness; and economical, versatile, and simple operation for removing trace amounts of metal ions. Therefore, it is important to fabricate such kind of adsorbents that have the efficacy to remove both organic dyes and lead-containing inorganic water pollutants simultaneously.

In recent time, nanoscience and nanotechnology have significant potential for remediation of environmental hazards. Different nanoadsorbents such as activated carbon,[4] layered double hydroxide,[5] zeolite,[6] iron-based nanoadsorbents,[7] etc. have been widely used for decontamination of water. Meng et al. reported a hybrid Si−C−N material for selective adsorption of an organic dye.[8] Poly(1-vinylimidazole) ionic liquid-modified graphene showed high adsorption capacity for methyl blue (MB).[9]

Porous carbon and carbonaceous materials are popular adsorbents for their large surface-to-volume ratio and high mechanical strength. Recently, new-generation N-doped carbons have been found to be interesting materials because of their superior physical and chemical properties as compared to those of their undoped counterparts. Accordingly, a wide range of applications are anticipated for these nitrogen-doped carbon materials such as anodes in high-performance lithium ion batteries,[10] high-performance supercapacitors,[11] etc. A nitrogen-

Received: June 6, 2018
Accepted: August 3, 2018
Published: August 24, 2018

DOI: 10.1021/acsomega.8b01252
ACS Omega 2018, 3, 9888−9898

doped carbon material can provide a large number of anchoring sites for adsorption of positive-charged metal ions due to electronegativity difference between N and C atoms.[12] Hence, it is necessary to develop and investigate nitrogen-doped carbon materials as an adsorbent to be exploited for removing toxic pollutants from water.

Nitrogen-doped carbon materials have been used for the removal of water contaminants. Recently, a N-doped carbon quantum dot−magnetite nanocomposite was exploited for adsorption of methylene blue from waste water.[13] The N-doped carbon synthesized from ionic liquid@ZIF 8 was used for the removal of herbicides from water.[14] Perez-Aguilar et al. reported the adsorption of Cd and Pb by N-doped multiwall carbon nanotubes prepared by the chemical vapor deposition process.[15] Nitrogen-doped magnetic carbon nanoparticles have been used for the removal of Cr^{3+} ions from water.[16] For the removal of toxic metal ions from water, N-doped carbon nanofibers were used.[17] A nitrogen-doped carbon xerogel was utilized for decontamination of water by removing heavy metal ions.[18]

With the above motivation, the main goal of the present research study is to synthesize highly porous nitrogen-doped carbon materials prepared using melamine and triblock copolymers (TBCs) and investigation of their performance as an adsorbent for the removal of both organic dye, methylene blue (MB), and inorganic pollutant, lead (Pb), from contaminated water. This study is significant for the fabrication of a suitable adsorbent, which could be applicable for the removal of multicomponent water pollutants, both organic dyes and inorganic toxic metal ions.

RESULTS AND DISCUSSION

Material Characteristics. Figure 1 shows the Raman spectra of samples CNF108, CNF127, and CNP123. The

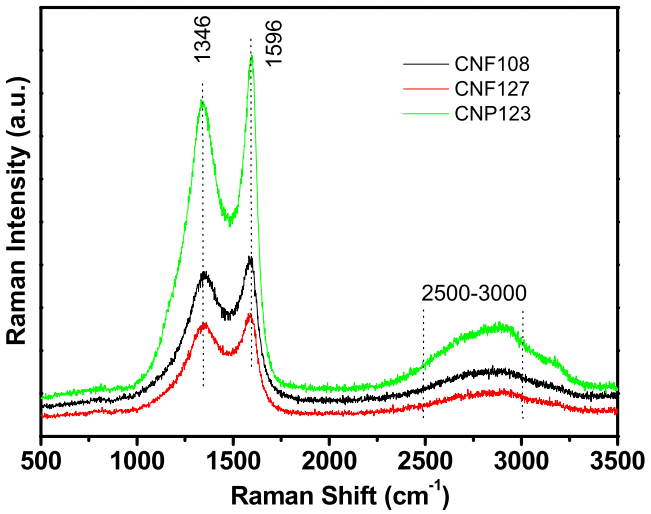

Figure 1. Raman spectra of nitrogen-doped nanoporous carbon nanospheroid (N@CNS) samples.

disorder structure of N-doped carbon materials is confirmed by the appearance of peak at 1346 cm^{-1} (D band), whereas the band at 1596 cm^{-1} is due to the sp^2-hybridized C−C bond in-plane stretching vibration (G band).[19,20] The broad band appeared at around 2500−3000 cm^{-1} is considered as a G″ band, i.e., overtone of the D band induced by disorder.[21] It is to be noted that there are no significant changes in Raman bands of the three different samples, CNF108, CNF127, and CNP123.

Figure 2 shows the N_2 adsorption−desorption isotherms of (a) CNF108, (b) CNF127, and (c) CNP123, indicating a pseudo-type-1 isotherm. The pore size distributions of the samples determined by the Barrett−Joyner−Halenda (BJH) method are shown in Figure 3, whereas the pore size distributions determined by the density functional theory (DFT) method are revealed in the insets of the corresponding figures. It is noticed that the mesopores generated in the samples are in the range of 3−4 nm, whereas bi- or trimodal distributions of micropores are observed for all of the samples. Table 1 depicts the surface area, pore volume, and pore size data of CNF108, CNF127, and CNP123. Interestingly, the sample CNF127 exhibits the highest Brunauer−Emmett−Teller (BET) surface area (773.4 m^2/g) having a pore volume of 0.877 cm^3/g. The total BET surface area comprises micropore surface area (545.5 m^2/g) and mesopore surface area (228 m^2/g). The surface area follows the order CNF127 > CNF108 > CNP123. However, the pore volume of CNP123 is found to be higher than that of CNF108, which is due to the presence of abundance mesoporosity in the former sample, contributing the higher pore volume. The pore size of all of the samples does not changed significantly.

The X-ray photoelectron spectroscopy (XPS) spectra of the products in full spectrum are shown in Figure 4a. This indicates the presence of C 1s, N 1s, and O 1s. The C 1s core level is deconvoluted into three subpeaks positioned around the binding energies of 284.6, 285.1, and 287.8 eV (Figure 4b). It is found that the position of the C 1s line assigning to the C−C bond is shifted from 284.4 to 284.6 eV due to nitrogen doping. After deconvolution, two additional peaks appear at around 285.1 and 287.87 eV. The sharp peak with the binding energy of 285.1 eV is attributed to the sp^2 C═N bonds, and the broad peak at 287.87 eV is attributed to sp^3 C−N bonds.[22] The high-resolution deconvoluted spectrum of N 1s is shown in Figure 4c−e for the samples CNF108, CNF127, and CNP123, respectively. The deconvoluted N 1s spectra render two distinguishable peaks with binding energies of 398.33 and 400.7 eV. The peaks at 398.33 and 400.7 eV are attributed to the pyridinic nitrogen or sp^2-hybridized nitrogen (C−N═C) and sp^3-hybridized nitrogen (C−N), respectively.[23−25] The above results confirm that in the nitrogen-doped carbon sample (N@CNS), nitrogen interacts with carbon via double and single bonds with sp^2- and sp^3-hybridized states, respectively. It is worth noting that for different co-polymer-modified N@CNS samples, the C 1s and N 1s peak positions remain unchanged. However, the atomic % values of doped nitrogen obtained from XPS results were found to be 4.05, 5.40, and 4.50 for the samples CNF108, CNF127, and CNP123, respectively.

Microstructural features of the samples were studied by field emission scanning electron microscopy (FESEM) (Figure 5) and transmission electron microscopy (TEM) (Figure 6). Figure 5 reveals the FESEM microstructures of the products CNF108, CNF127, and CNP123, and the arrow marks represent the images with higher magnifications. The carbon nanospheroids of size 50−200 nm were highly aggregated. The high surface charge of the particles due to the polarity difference between carbon and nitrogen atoms in N@CNS facilitates agglomeration of the particles. The TEM images (Figure 6) show that the particles are arranged in a chainlike fashion. The TEM images with a higher magnification reveal the pores in the products. The energy dispersive X-ray spectroscopy (EDS)

DOI: 10.1021/acsomega.8b01252
ACS Omega 2018, 3, 9888−9898

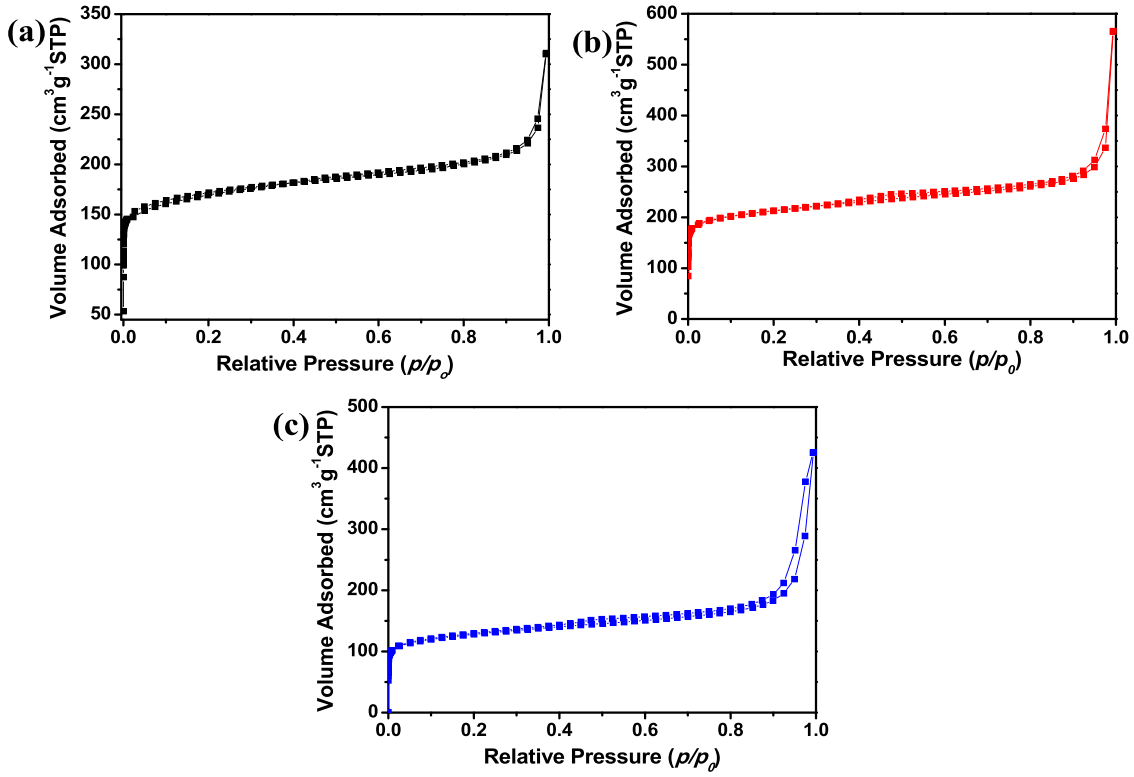

Figure 2. N_2 adsorption−desorption isotherms of N@CNS samples: (a) CNF108, (b) CNF127, and (c) CNP123.

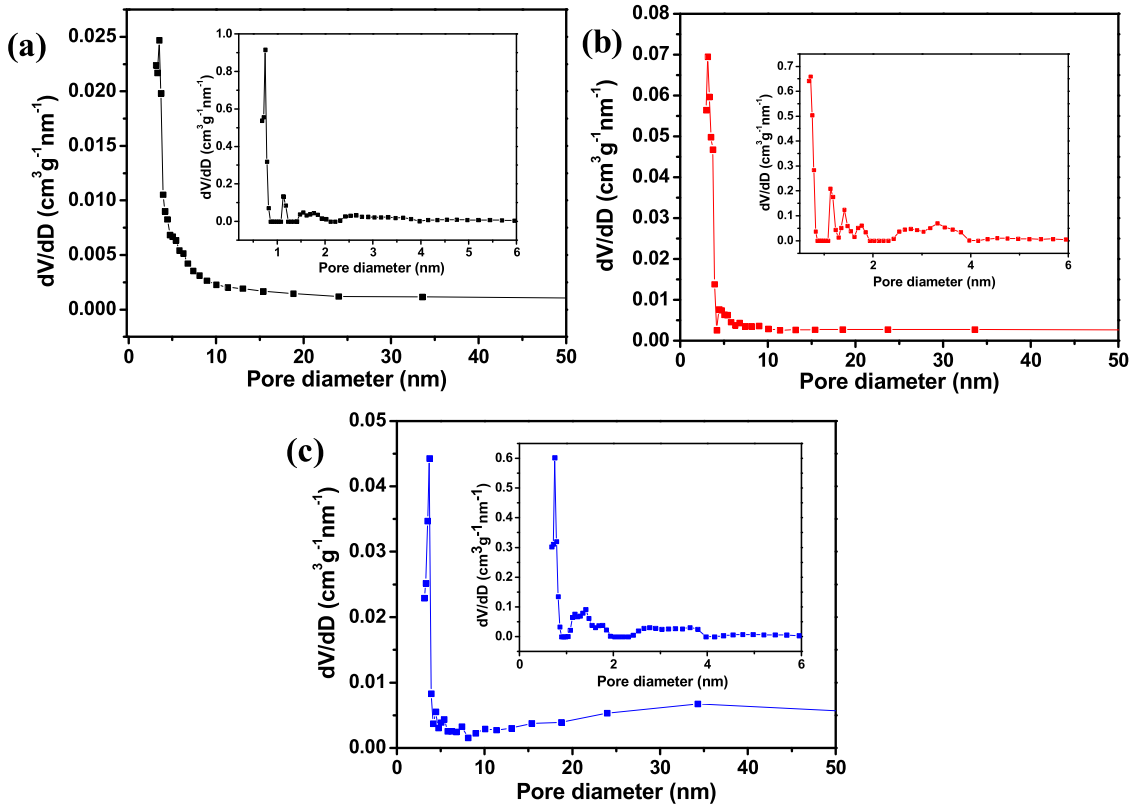

Figure 3. BJH pore size distributions of N@CNS: (a) CNF108, (b) CNF127, and (c) CNP123; insets reveal DFT pore size distributions.

analysis of the three samples reveals the presence of nitrogen in nitrogen-doped carbon samples (N@CNS).

Dye Adsorption Study. *Selective Adsorption of Dye.* To study the selective adsorption capacity of the synthesized products, the cationic dye MB and anionic dye methyl orange (MO) were used with an equal concentration of 10×10^{-2} mM. Figure 7 shows the UV−vis spectral analysis for the selective dye adsorption of MB and MO onto the samples. For comparison,

DOI: 10.1021/acsomega.8b01252
ACS Omega 2018, 3, 9888−9898

Table 1. Textural Properties of the Samples

	surface area (m^2/g)[a]				
sample ID	S_{BET}	$S_{micropore}$	$S_{mesopore}$	$V_{p\text{-}total}$ (cm^3/g)[b]	pore diameter (nm)
CNF108	624.7	497	127.7	0.482	3.50
CNF127	773.4	545.4	228	0.877	3.14
CNP123	462.6	255.6	207	0.660	3.71

[a]BET surface area. [b]Pore volume.

Figure S1, Supporting Information (SI) shows the UV−vis spectrum of each dye MO and MB separately for sample CNF127. To further investigate the selective removal of the dyes having the same charge, the cationic dyes methylene blue (MB) and methyl violet (MV) with a concentration of 5×10^{-2} mM each were used for sample CNF127. Figure S2, SI, shows (a) UV−vis spectral analysis and (b) bar diagram (time vs adsorption %) of the adsorption of two cationic dyes MB and MV for sample CNF127. This reveals that adsorption % for MV is slightly higher than that of MB up to 40 min, followed by their comparable adsorption for 50 min. However, after 60 min, adsorption % values for MB and MV were found to be 84 and 83.5%, respectively. It is worth noting that adsorption % for MB in the presence of MV is slightly less than that in the presence of MO because of competitive adsorption of both the cationic dyes in the former dyes (MB and MV).

The adsorption of MB onto the nitrogen-doped carbon nanospheroids (N@CNS) is due to electrostatic interaction between nitrogen lone pairs in N@CNS and the cationic dye, MB. On the other hand, due to the presence of electron cloud in both the anionic MO dye molecules and N@CNS having sp^2-hybridized nitrogen, the adsorption of MO seldom occurs onto N@CNS. The molecular sizes of hydrated MB and MO in aqueous solution are 11.2[26] and 26.14 Å,[27] respectively. Therefore, it is evident that the adsorption of MB is more facile than that of MO due to the smaller size of the former dye. The adsorption capacity for MB of the three samples follows the order CNF127 > CNP123 > CNF108, which corroborated with the mesoporosity of the corresponding samples (Table 1). The maximum nitrogen content in the CNF127 sample also contributed to the faster adsorption of MB.

It was noticed that CNF127 shows a higher adsorption capacity for MB. The adsorption parameters like contact time, adsorbent (MB) concentration, and temperature were varied for determining the adsorption capacity of CNF127. Figure 8a,b shows the UV−vis spectral study and C_t/C_0 vs time plot for the adsorption of MB on CNF127, respectively. The adsorption of MB is high at the initial stage of adsorption, and after that, the adsorption capacity decreases with time. At the initial stage of adsorption, a large number of adsorption sites are available in the adsorbent (CNF127), causing the rapid adsorption of MB. The adsorption capability (q_t) of the sample was calculated using eq 1, and the q_t vs time plot is shown in Figure 8c. It shows that after 40 min of adsorption equilibrium is reached, rendering about 98% adsorption.

To understand the adsorption mechanisms, the adsorption kinetics of MB on CNF127 revealing the highest adsorption capacity was carried out by employing three kinetic models. The experimental data were fitted with pseudo-first-order (eq 1) and pseudo-second-order (eq 2) models.

$$\ln(q_e - q_t) = -k_1 t + \ln q_e \quad (1)$$

$$t/q_t = 1/k_2 q_e^{\ 2} + (1/q_e)t \quad (2)$$

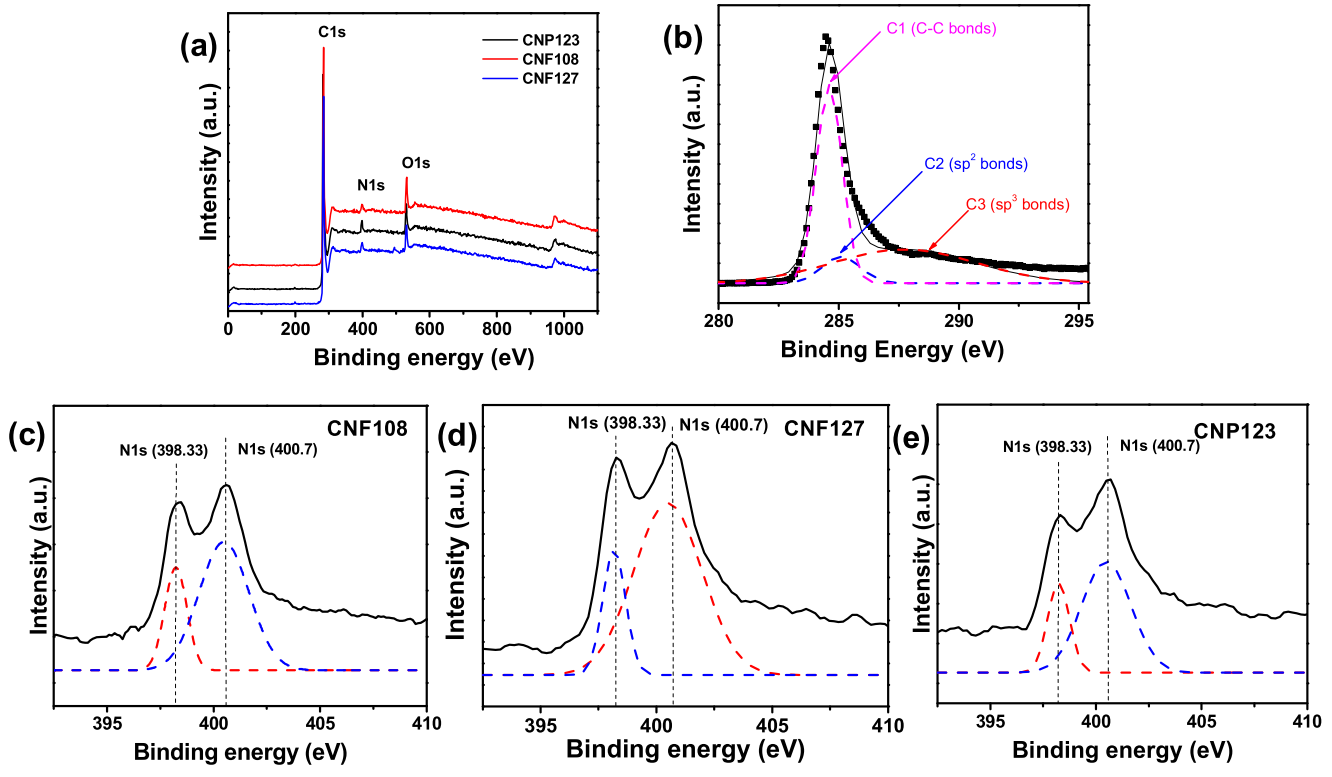

Figure 4. XPS spectra of the N@CNS samples (a) in full spectrum; and (b) deconvoluted C 1s spectra and deconvoluted N 1s spectra of (c) CNF108, (d) CNF127, and (e) CNP123.

DOI: 10.1021/acsomega.8b01252
ACS Omega 2018, 3, 9888−9898

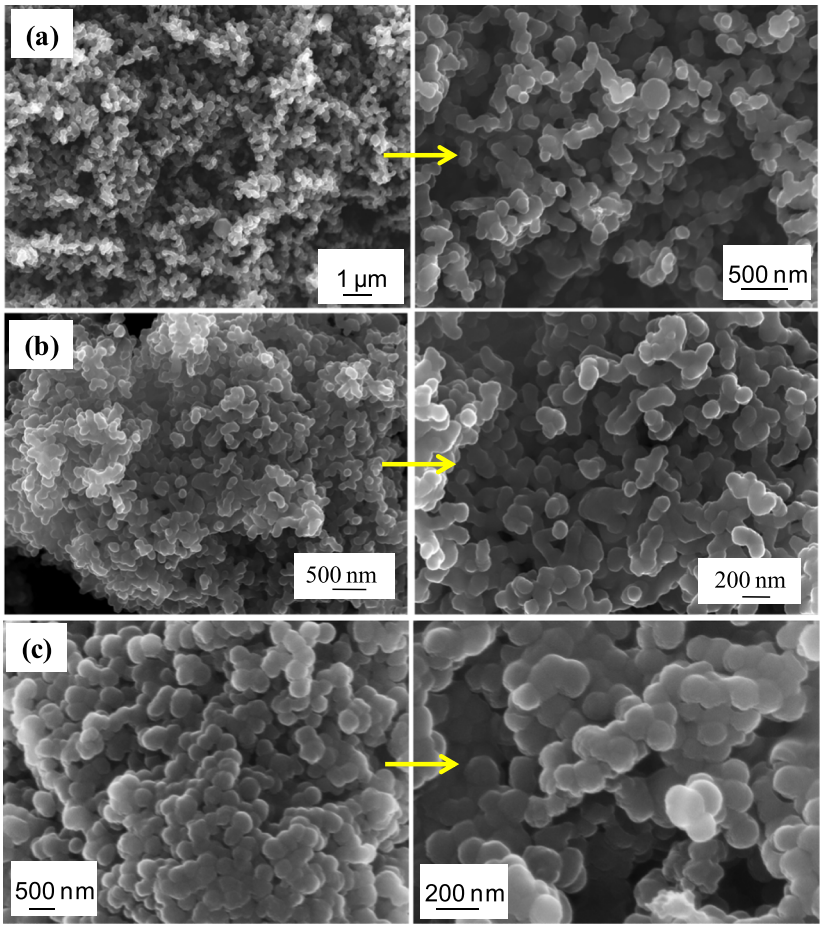

Figure 5. FESEM microstructures of N@CNS: (a) CNF108, (b) CNF127, and (c) CNP123.

where q_e and q_t (mg/g) are the amounts of pollutants adsorbed at equilibrium and at time t (min), respectively, k_1 (min^{-1}) is the Lagergren pseudo-first-order and k_2 (g/mg/min) is the corresponding second-order rate constant, and t (min) is the contact time between the adsorbent and adsorbate. The fitted plots for pseudo-first-order and pseudo-second-order models are shown in Figures S3 and S4 (SI), respectively. All of the experimental data obtained from fitted first-order and second-order models is summarized in Table 2. The R^2 (correlation coefficient) values of 0.999 confirm that MB adsorption on CNF127 occurs with the pseudo-first-order kinetics model.

For a better perceptive of the adsorption mechanism with diffusion, the intraparticle diffusion model was examined by applying the Weber and Morris equation

$$q_t = k_{di}\sqrt{t} + C_i \quad (3)$$

where k_{di} is the intraparticle rate constant (mg/g $min^{1/2}$), t is the time (min), and C_i (mg/g) is a constant related to the thickness of the boundary layer. Figure S3 (SI) shows q_t vs $\sqrt{t}$ plots representing trilinear regimes of three successive adsorption steps for MB. The sharp rise in the 1st linear region of adsorption involves the instantaneous adsorption where a high concentration of MB is the driving force of diffusion. The second linear region relates relatively slow and steady which is the rate-determining step attributing intraparticle diffusion of MB onto the adsorbent pores.[28] Finally, due to the presence of low concentration of dye molecules, the intraparticle diffusion rate decreases and an equilibrium stage is reached. All of the experimental data obtained from the trilinear plot (Figure S5, SI) is summarized in Table 2.

To evaluate the adsorption capacity, the adsorption isotherms are obtained by varying the MB concentrations in solution. It was observed that the amount of equilibrium adsorption (q_e) increases with increasing equilibrium concentration (C_e) of MB up to 25×10^{-2} mM (Figure 9). The q_e and C_e are fitted with the two isotherm models (Langmuir and Freundlich) for understanding the interaction between CNF127 and MB. Linear plots of Langmuir and Freundlich isotherm models are revealed in Figure S6a,b, SI, respectively. The correlation coefficient (R^2) obtained for the fitted plot of the Langmuir isotherm (R^2 = 0.999) is higher than that for the Freundlich isotherm (R^2 = 0.959). This demonstrates that the Langmuir model is fitted satisfactorily, implying the monolayer adsorption of dye molecules onto CNF127.[29] According to the Langmuir model, the maximum adsorption capacity of CNF127 for MB adsorption was found to be 73 mg/g.

The adsorption capacity of MB (5×10^{-2} mM) in the presence of two electrolytes, namely, calcium nitrate and magnesium nitrate with a concentration of 10 mg/L each, was studied (Figure S7, SI). This showed that about 1 and 10% adsorption occurred for calcium nitrate and magnesium nitrate, respectively, whereas about 90% of MB was adsorbed on CNF127. The electrolytes could not effect significantly to change the adsorption of MB.

To evaluate the temperature effect on the adsorption of MB, the adsorption experiment was carried out with varying temperature keeping the initial concentration of MB as 15 ×

DOI: 10.1021/acsomega.8b01252
ACS Omega 2018, 3, 9888−9898

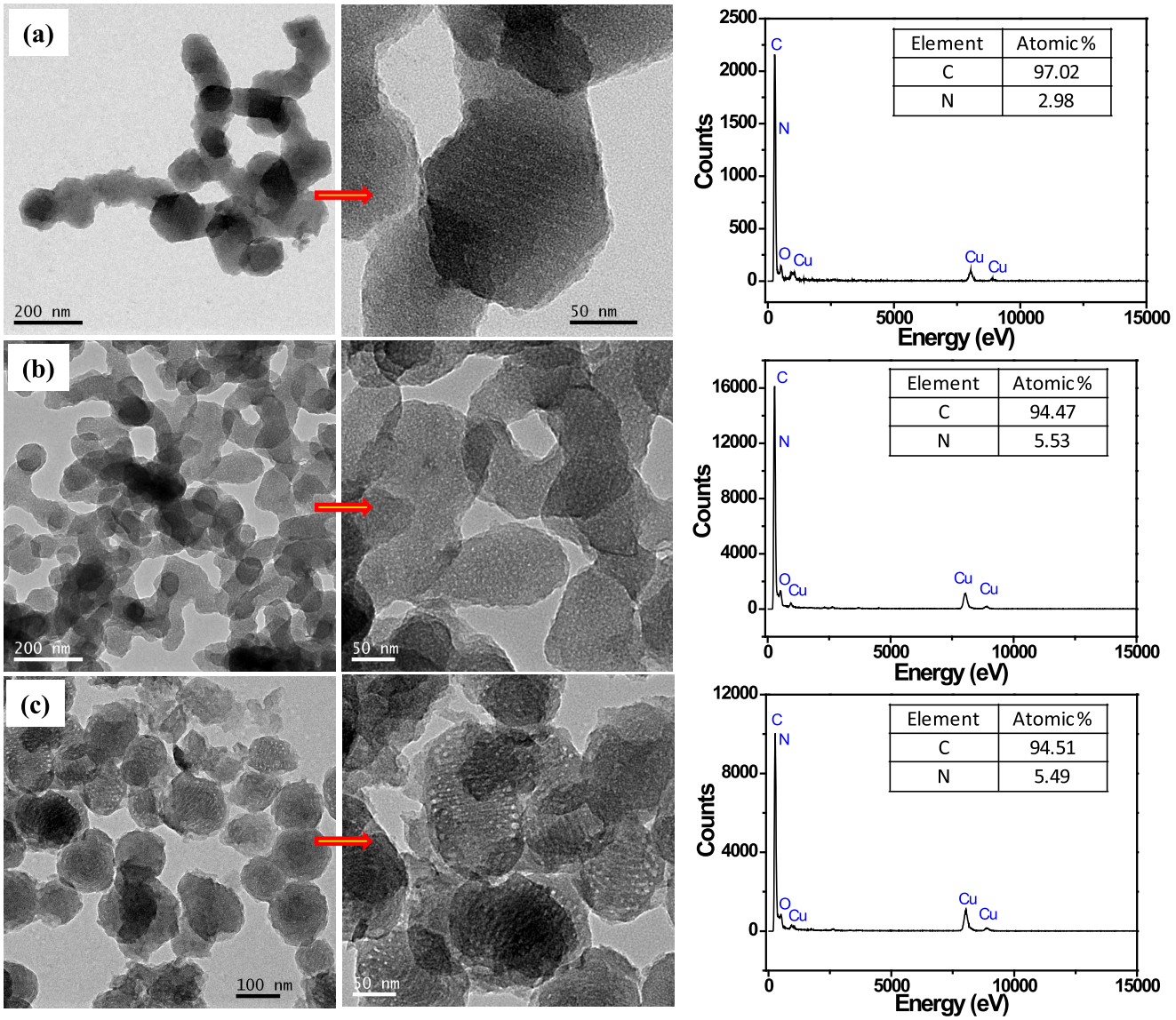

Figure 6. TEM images and EDS of N@CNS samples: (a) CNF108, (b) CNF127, and (c) CNP123.

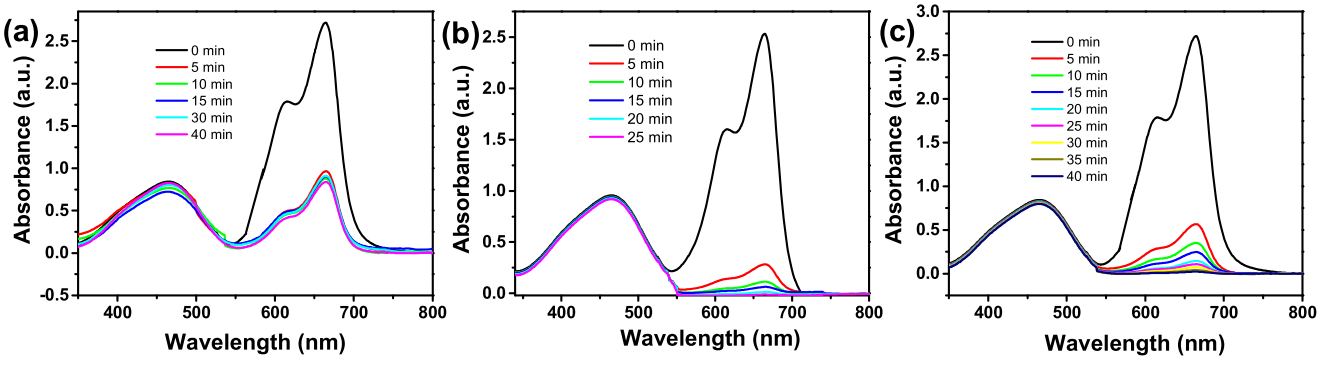

Figure 7. UV−vis spectral analysis for selective dye adsorption for N@CNS samples: (a) CNF108, (b) CNF127, and (c) CNP123.

10^{-2} mM. Figure 10 shows the bar diagram of MB adsorption, q_t, vs temperature. With an increase in temperature, MB adsorption increased. This suggests that with an increase in temperature, diffusion of MB through the external laminar layer into the pores of the sample increased, resulting in an increase in the adsorption rate.[30] The CNF127 sample shows the maximum adsorption for MB (94.93 mg/g) at 338 K.

The thermodynamic parameters such as Gibbs free energy change ($\Delta G°$), enthalpy change ($\Delta H°$), and entropy change ($\Delta S°$) were calculated using the following equation

DOI: 10.1021/acsomega.8b01252
ACS Omega 2018, 3, 9888−9898

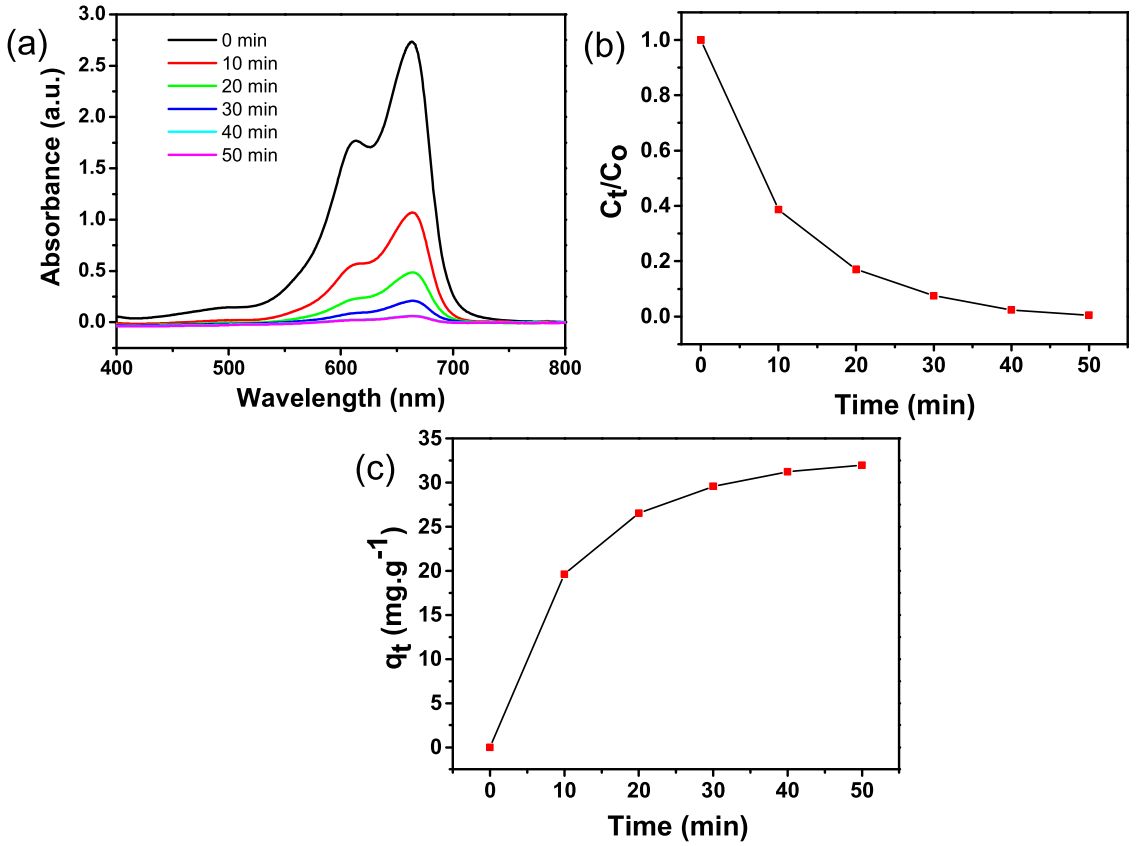

Figure 8. (a) UV−vis spectral study for MB adsorption with time for CNF127, (b) C_t/C_0 vs time plot, and (c) adsorption capacity vs time plot.

Table 2. Parameters of the Adsorption Isotherm and Kinetic Rate Models for the Adsorption of MB

pseudo-first-order kinetics	$\ln(q_e - q_t) = -k_1 t + \ln q_e$	$k_1 = 0.097\ \text{min}^{-1}$ $q_e = 31.28$ mg/g $R^2 = 0.999$		
pseudo-second-order kinetics	$t/q_t = 1/k_2 q_e^2 + (1/q_e)t$	$k_2 = 0.0095$ (g/mg/min) $q_e = 32.62$ mg/g $R^2 = 0.9873$		
intraparticle diffusion kinetic	$q_t = k_{di}\sqrt{t} + C_i$	$k_{d1} = 6.2081$ $k_{d2} = 2.552$ $k_{d3} = 0.151$	$C_1 = 2.512$ $C_2 = 15.272$ $C_3 = 30.608$	$(R_1)^2 = 1$ $(R_2)^2 = 0.972$ $(R_3)^2 = 0.764$
Langmuir isotherm	$C_e/q_e = C_e/q_m + 1/K_L \times q_m$	$K_L = 0.201$ $q_m = 73$ mg/g $R^2 = 0.999$		
Freundlich isotherm	$\log q_e = \log K_F + 1/n_F \log C_e$	$K_F = 26.29$ $n_F = 5.426$ $R^2 = 0.959$		

$$K_d = q_e/C_e \quad (4)$$

$$\ln K_d = \Delta S^\circ/R - \Delta H^\circ/RT \quad (5)$$

$$\Delta G^\circ = -RT \ln K_d \quad (6)$$

where K is the thermodynamic equilibrium constant, R is the universal gas constant (8.314 J/mol/K), and T is the temperature (K). The values of ΔH° and ΔS° are obtained from the slope and intercept of the plot of $\ln K_d$ vs $1/T$, respectively (Figure S8, SI). The values of ΔG°, ΔH°, and ΔS° for the adsorption process at 25 °C (298 K) are shown in Table 3. The negative ΔG° value signifies that MB adsorption by CNF127 is spontaneous. The adsorption process is exothermic as indicated by the negative ΔH° value, and positive ΔS° value signifies the increases in randomness at the solid−liquid interface during adsorption.[31]

To examine the suitability of the sample CNF127 for the removal of MB in municipality water (real matrix), the adsorption experiment is further carried out in municipality water samples. The simulation experiments were performed in municipality water system with different initial concentrations of MB (10×10^{-2}, 15×10^{-2} and 25×10^{-2} mM). The adsorption capacity (mg/g) of CNF127 for MB in municipality water and deionized water was found to be comparable (Figure S9, SI).

Adsorption of Pb(II) Ions. The synthesized samples (CNF108, CNF127, and CNP123) also have the significant potential for removing Pb(II) ions (hydrated radius of Pb(II): 2.61 Å[32]) from waste water. To study the adsorption capacity

DOI: 10.1021/acsomega.8b01252
ACS Omega 2018, 3, 9888−9898

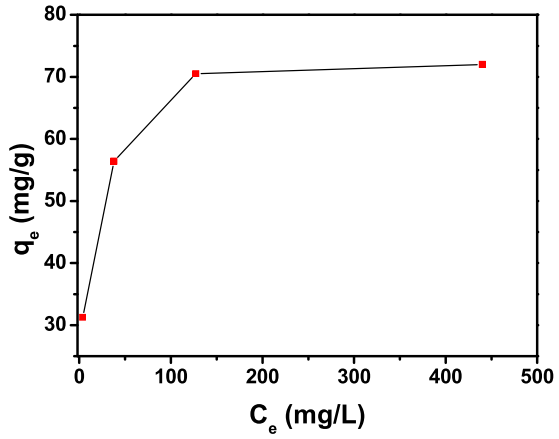

Figure 9. Adsorption isotherm for different concentrations of MB for CNF127.

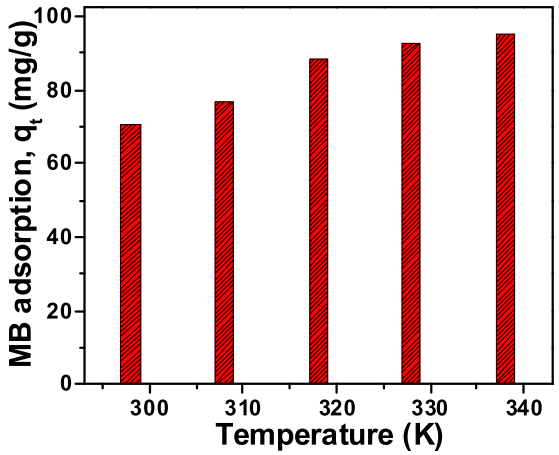

Figure 10. MB adsorption with temperature for CNF127.

Table 3. $\Delta H°$, $\Delta S°$, and $\Delta G°$ Values for MB Adsorption by CNF127

$\Delta H°$ (J/mol)	$\Delta S°$ (J/mol/K)	$\Delta G°$ (kJ/mol)
−74485.55	300.10	−15.678 at 298 K
		−17.153 at 308 K
		−20.632 at 318 K
		−23.751 at 328 K
		−26.705 at 338 K

toward Pb(II) ions removal, 5 mg of sample was utilized for 50 ppm Pb(II) ion adsorption at different time intervals. Figure 11 shows that within 5 min the adsorption of Pb(II) ions took place rapidly, showing the adsorption capacities of 62.5, 91.4, and 71.7 mg/g for samples CNF108, CNF127, and CNP123, respectively. This indicates that a large number of active adsorption sites are available at the first stage. After that, the adsorption of Pb(II) ions continues slowly, achieving maximum adsorption at 120 min. The maximum % adsorption of Pb(II) followed in the order of CNF127 (99.82%) > CNF108 (98.74%) > CNP123 (91.82%); this trend corroborates with the BET surface area of the corresponding samples. It is clear that with a higher BET surface area of CNF127, the available active adsorption sites are abundant, leading to the higher rate of Pb(II) ion adsorption. Figures S10 and S11, SI, show pseudo-first-order and pseudo-second-order kinetic models. The parameters q_t, k_1, k_2, and R^2 are summarized in Table S1, SI. For all of the samples, pseudo-

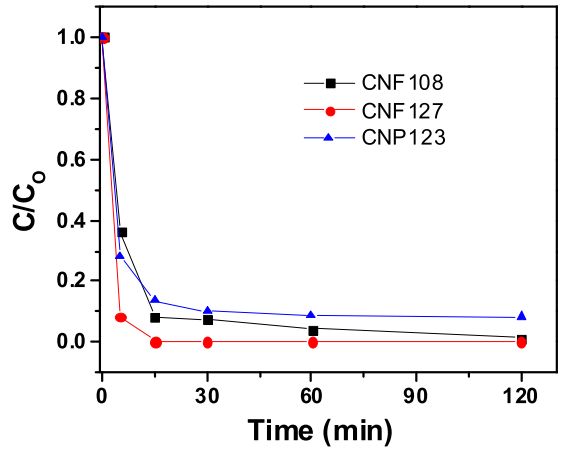

Figure 11. C/C_0 vs time plot for Pb(II) adsorption by N@CNS.

second-order kinetics is a well-fitted model, as shown by the R^2 values (Table S1, SI). This indicates that the chemisorption process is the rate-determining step.

To evaluate the adsorption capacity for Pb(II) ions in the presence of different electrolytes, the experiment was carried out in the presence of $Ca(NO_3)_2$ and $Mg(NO_3)_2$. Figure S12, SI, shows (a) adsorption of Pb(II) ions in the absence and presence of Ca(II) and Mg(II) ions and (b) relative adsorption of Pb(II) ions in the presence of Ca(II) and Mg(II) ions. This shows that in the presence of Ca(II) and Mg(II) ions the adsorption % of Pb(II) ions decreased as about 8, 10, and 11% for the samples CNF127, CNF108, and CNP123, respectively. However, in the presence of Ca(II) and Mg(II) ions, the adsorption of Pb(II) ions was 92, 88.9, and 80.3% for CNF127, CNF108 and CNP123, respectively. The adsorption capacity of the multi-component metal ions followed the trend Pb(II) > Mg(II) > Ca(II), which is related to their electronegativity values[33] (Pauling's scale) (Pb(II) (2.33) > Mg(II) (1.31) > Ca(II) (1.00)). In N@CNS, the sp^2-hybridized nitrogen having a lone pair electron as well as delocalized π electron facilitates more Pb(II) ion adsorption due to its higher electronegativity compared to that of Mg(II) and Ca(II) ions.

The proposed adsorption mechanism is shown in Figure 12. The adsorption of pollutants (MB dye and Pb(II) ion) onto the surface of N@CNS samples could be governed by the electrostatic interactions. On the basis of the XPS study, it is clear that nitrogen in N@CNS is in sp^2-hybridized as well as sp^3-

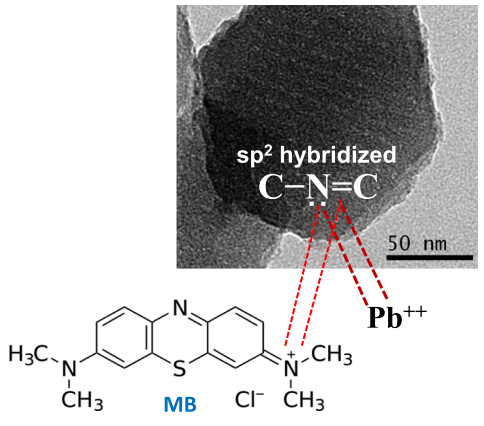

Figure 12. Adsorption mechanism for MB and Pb(II) by N@CNS samples.

DOI: 10.1021/acsomega.8b01252
ACS Omega 2018, 3, 9888−9898

Scheme 1. Schematic Representation for the Formation of N@CNS

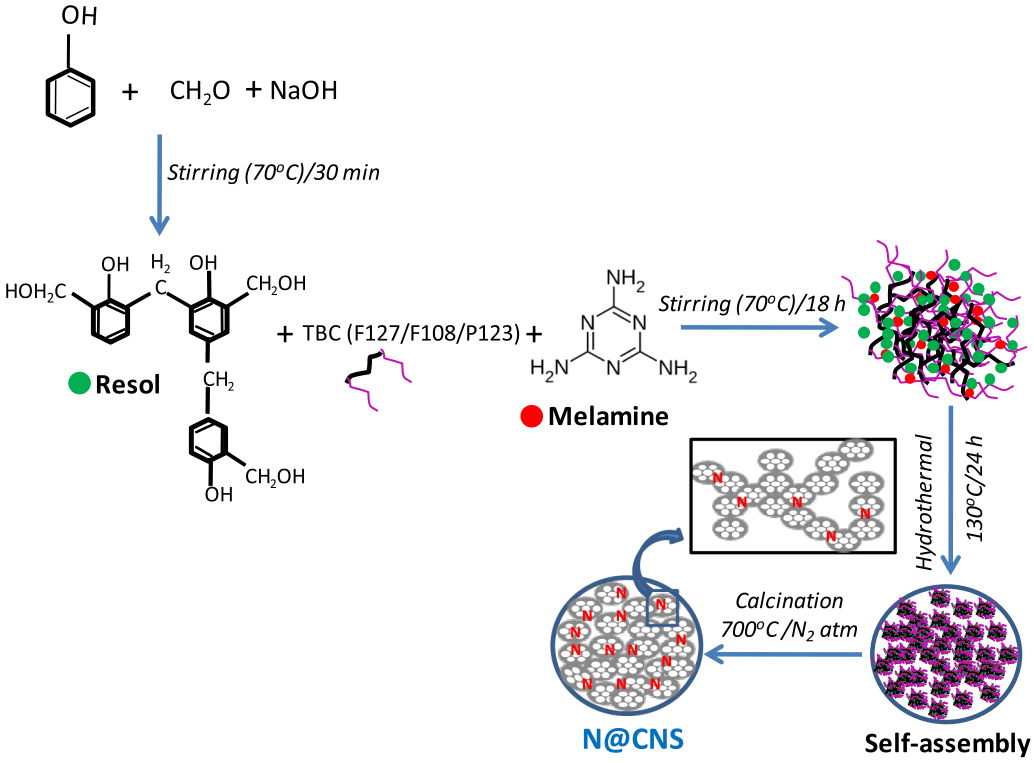

hybridized states. In the sp^2-hybridized state of nitrogen in N@CNS, both the lone pair electron in nitrogen and delocalized π electrons in the N=C bond electrostatically interact with cationic dye MB. It is worth noting that the presence of sp^2-hybridized carbon in hybrid Si−C−N[8] and poly(1-vinylimidazole) ionic liquid-modified graphene[9] exhibit a higher adsorption capacity for MB. For adsorption of Pb(II) ions, it is understood that in N@CNS the sp^2-hybridized nitrogen having a lone pair electron as well as delocalized π electrons could be available to donate the vacant 6p orbital of Pb(II) ions. Thus, the positively charged dye, MB, and Pb(II) ions were readily adsorbed onto N@CNS via electrostatic attractions. With increasing N sites of N@CNS samples, the adsorption capacity increases. Accordingly, the sample CNF127 having a higher amount of N content (5.4 atom %) renders maximum adsorption for both MB dye and Pb(II) ions. On the other hand, the anionic dye, MO, could not be adsorbed onto the N@CNS samples due to the presence of electron cloud in both the anionic MO dye molecules and N@CNS. It is inferred that the synthesized nitrogen-doped carbon nanospheroids (N@CNS) could be used for selective adsorption of organic dye and positively charged cations from contaminated water.

CONCLUSIONS

In summary, nitrogen-doped nanoporous carbon nanospheroids were prepared using various block copolymers and melamine. The synthesized products contain both micropores and mesopores, and the BET surface area follows the order CNF127 > CNF108 > CNP123 for F127-, F108-, and P123-modified samples, respectively. The microstructural study confirms agglomerated nanospheroids due to the presence of their high surface charge. The XPS study confirms that N atoms in nitrogen-doped carbon are in sp^2-hybridized as well as sp^3-hybridized states. In the sp^2-hybridized state of nitrogen in the product, both the lone pair electron in nitrogen and delocalized π electrons in C−N=C electrostatically interact with cationic dye MB, rendering its selective adsorption in the presence of anionic dye MO. For MB adsorption, the adsorption capacity follows the order CNF127 > CNP123 > CNF108, which corroborates with the N content in the respective samples. Similarly, Pb(II) adsorption is facilitated because the sp^2-hybridized nitrogen having a lone pair electron as well as delocalized π electrons in nitrogen-doped carbon could be available to donate the vacant 6p orbital of Pb(II) ions. The maximum % of Pb(II) adsorption followed in the order CNF127 (99.82%) > CNF108 (98.74%) > CNP123 (91.82%); this trend corroborates with the BET surface area of the corresponding samples. The present work is significant for designing the synthesis of nitrogen-doped carbon nanospheroids for the removal of different cationic organic dyes and toxic metals from waste water via an environmentally friendly process.

EXPERIMENTAL SECTION

Materials. Merck, India (formaldehyde, phenol, methylene blue (MB), methyl orange (MO), methyl violet (MV), magnesium nitrate, calcium nitrate, lead nitrate, and sodium hydroxide) and Sigma-Aldrich (melamine and triblock copolymers) products were used.

Procedure. Phenol (600 mg) was added into a mix solution of formaldehyde (2.1 mL) and NaOH (15 mL 0.1 M) under stirring at 70 °C/30 min. F108, F127, and P123 (0.07 mmol, 15 mL) each was poured separately to the former solution. After stirring for 2 h, 2.66 g of melamine in water (50 mL) was added. Stirring was continued for 15−18 h. Deionized water (56 mL) was added into 18 mL of prepared solution each, and it was treated hydrothermally at 130 °C/24 h. The hydrothermally synthesized products were heated in a tube furnace by flowing N_2 (40 mL/min) at 700 °C/3 h. The sample IDs of synthesized

DOI: 10.1021/acsomega.8b01252
ACS Omega 2018, 3, 9888−9898

nitrogen-doped carbon nanospheroids (N@CNS) were CNF108, CNF127, and CNP123 for the different copolymers F108, F127, and P123, respectively. Scheme 1 shows a tentative formation mechanism for the preparation of N-doped porous carbon nanospheroids. During synthesis, formaldehyde reacts with phenol in alkaline medium to form polymeric resol (water-soluble phenolic resin). In the presence of triblock copolymers (TBC, F127/F108/P123), resol and melamine form micelles in which the TBC interacts with the hydroxyl groups of resol and amino groups of melamine through hydrogen bonding. Under hydrothermal conditions at 130 °C/24 h, resol-TBC-melamine micelles self-assembled to form a yellowish product. After calcinations at 700 °C/3 h in a N_2 atmosphere, templated TBC and organic moieties are removed from the hydrothermally synthesized product, forming porous N@CNS particles.

The synthesized products were characterized by Raman spectroscopy (Renishaw spectrometer, 514 nm Ar laser), N_2 adsorption−desorption measurements (Quantachrome ASIQ MP), X-ray photoelectron spectroscopy (ULVAC-PHI), FESEM (Zeiss, Supra 35VP, Oberkochen, Germany), and TEM (Tecnai G2 30ST, FEI). UV−visible spectroscopy was performed by a UV−vis spectrophotometer (Jasco V-730).

Adsorption Experiment. The prepared sample (5 mg, N@CNS) was added into 10 mL solutions of MB with different initial concentrations in the range of 5×10^{-2} to 25×10^{-2} mM. After the specified time, the adsorbent was filtered and MB concentration in the solution was measured by a UV−vis spectrophotometer. The amount of MB removed by the samples, q_t (mg/g), was calculated using the following equation

$$q_t = (C_0 - C_t) \times V/m \tag{7}$$

where q_t (mg) is the amount of MB adsorbed per gm of adsorbent at time t, C_0 (at initial time) and C_t (at time t) are the MB concentrations, and V (mL) and m (gm) are the adsorbent volume and adsorbent mass, respectively.

For kinetic study, 5×10^{-2} mM MB (10 mL) was mixed with 5 mg of N@CNS samples under stirring for different times. At a desired time interval, the concentration of MB in the solution was measured by a UV−vis spectrophotometer. Pseudo-first-order, pseudo-second-order, and intraparticle diffusion models were used to fit the kinetic data.

To determine the surface properties of the adsorbent and interactions between the adsorbent and adsorbate, adsorption data were fitted with Langmuir and Freundlich models. The Langmuir equation is expressed as

$$q_e = q_m b C_e/(1 + K_L C_e) \tag{8}$$

The linear form of the Langmuir isotherm is represented as

$$C_e/q_e = C_e/q_m + 1/K_L \times q_m \tag{9}$$

Here, q_e (mg/g) represents the amount of adsorbed MB (mg) per gm of N@CNS samples, q_m (mg/g) is the equilibrium adsorption capacity (maximum), C_e (mg/L) is the MB left unadsorbed at equilibrium, and K_L is the adsorption constant. By plotting C_e/q_e vs C_e, q_m and K_L can be known from the slope and intercept, respectively.

Freundlich isotherm is expressed as

$$\log q_e = \log K_F + 1/n_F \log C_e \tag{10}$$

where K_F and n_F are the measures of adsorption capacity and adsorption intensity, respectively, and K_F and $1/n_F$ are known from the intercept and slope of the $\log C_e$ vs $\log q_e$ graph, respectively.

The adsorption experiment for Pb(II) was studied by adding 5 mg of samples into 10 mL of 50 ppm Pb(II) ion solution (Pb(II) concentrations were measured by inductively coupled plasma atomic emission spectroscopy at different time intervals).

■ ASSOCIATED CONTENT

Supporting Information

The Supporting Information is available free of charge on the ACS Publications website at DOI: 10.1021/acsomega.8b01252.

UV−vis spectra for MO and MB adsorption; UV−vis and bar diagram for MB and MV adsorption; pseudo-first-order, pseudo-second-order, and intraparticle diffusion kinetic plots for the adsorption of MB by CNF127; Langmuir (a) and Freundlich isotherms (b) of MB adsorption on CNF127; adsorption of MB in the presence of electrolytes; ln K_d versus $1/T$ plot for MB adsorption by CNF127; MB adsorption in municipality water and deionized water; pseudo-first-order and pseudo-second-order kinetic plots for the adsorption of Pb(II) by the N@CNS samples: (a) CNF108, (b) CNF127, and (c) CNP123; adsorption of Pb(II) ions with Ca(II) and Mg(II) ions; kinetics model parameters for Pb(II) ion adsorption (PDF)

■ AUTHOR INFORMATION

Corresponding Author

*E-mail: milan@cgcri.res.in. Tel: +91 33 2473 3496 (ext. 3516).

ORCID

Milan Kanti Naskar: 0000-0002-7447-4941

Notes

The authors declare no competing financial interest.

■ ACKNOWLEDGMENTS

The authors would like to acknowledge Dr K. Muraleedharan, Director of CSIR-CGCRI, for his kind permission to carry out this work. S.K. is thankful to AcSIR (CSIR) for granting her research fellowship (Grant No. 31/GATE/15(24)/2015-EMR-I).

■ REFERENCES

(1) Sarkar, C.; Bora, C.; Dolui, S. K. Selective Dye Adsorption by pH Modulation on Amine-Functionalized Reduced Graphene Oxide−Carbon Nanotube Hybrid. *Ind. Eng. Chem. Res.* **2014**, *53*, 16148−16155.

(2) Chattopadhyay, S.; Mishra, M. K.; De, G. Functionalized C@TiO_2 Hollow Spherical Architectures for Multifunctional Applications. *Dalton Trans.* **2016**, *45*, 5111−5121.

(3) Momčilović, M.; Purenović, M.; Bojić, A.; Zarubica, A.; Randelović, M. Removal of Lead (II) ions From Aqueous Solutions by Adsorption onto Pine Cone Activated Carbon. *Desalination* **2011**, *276*, 53−59.

(4) El-Wakil, A. M.; Awad, F. S. Removal of Lead From Aqueous Solution on Activated Carbon and Modified Activated Carbon Prepared From Dried Water Hyacinth Plant. *J. Anal. Bioanal. Tech.* **2014**, *5*, 1−14.

(5) Yanming, S.; Dongbin, L.; Shifeng, L.; Lihui, F.; Shuai, C.; Haque, M. A. Removal of Lead from Aqueous Solution on Glutamate Intercalated Layered Double Hydroxide. *Arabian J. Chem.* **2013**, *10*, S2295−S2301.

(6) Safinejad, A.; Goudarzi, N.; Chamjangali, M. A.; Bagherian, G. Effective Simultaneous Removal of Pb (II) and Cd (II) Ions By a New

DOI: 10.1021/acsomega.8b01252
ACS Omega 2018, 3, 9888−9898

Magnetic Zeolite Prepared from Stem Sweep. *Mater. Res. Express* **2017**, *4*, No. 116104.
(7) Liu, X.; Hu, Q.; Fang, Z.; Zhang, X.; Zhang, B. Magnetic Chitosan Nanocomposites: a Useful Recyclable Tool for Heavy Metal ion Removal. *Langmuir* **2009**, *25*, 3−8.
(8) Meng, L.; Zhang, X.; Tang, Y.; Su, K.; Kong, J. Hierarchically Porous Silicon−Carbon−Nitrogen Hybrid Materials Towards Highly Efficient and Selective Adsorption of Organic Dyes. *Sci. Rep.* **2015**, *5*, No. 7910.
(9) Zhao, W.; Tang, Y.; Xi, J.; Kong, J. Functionalized Graphene Sheets with Poly (ionic liquid) s and High Adsorption Capacity of Anionic Dyes. *Appl. Surf. Sci.* **2015**, *326*, 276−284.
(10) Yang, Y.; Jin, S.; Zhang, Z.; Du, Z.; Liu, H.; Yang, J.; Ji, H. Nitrogen-Doped Hollow Carbon Nanospheres for High-Performance Li-Ion Batteries. *ACS Appl. Mater. Interfaces* **2017**, *9*, No. 14180.
(11) Xiong, S.; Fan, J.; Wang, Y.; Zhu, J.; Yu, J.; Hu, Z.; et al. A Facile Template Approach to Nitrogen-doped Hierarchical Porous Carbon Nanospheres from Polydopamine for High-Performance Supercapacitors. *J. Mater. Chem. A* **2017**, *5*, 18242−18252.
(12) Reddy, A. L. M.; Srivastava, A.; Gowda, S. R.; Gullapalli, H.; Dubey, M.; Ajayan, P. M. Synthesis of Nitrogen-Doped Graphene Films for Lithium Battery Application. *ACS Nano* **2010**, *4*, 6337−6342.
(13) Tadesse, A.; Rama Devi, D.; Hagos, M.; Battu, G.; Basavaiah, K. Synthesis of Nitrogen Doped Carbon Quantum dots/Magnetite Nanocomposites for Efficient Removal of Methyl Blue Dye Pollutant from Contaminated Water. *RSC Adv.* **2018**, *8*, 8528−8536.
(14) Sarker, M.; Ahmed, I.; Jhung, S. H. Adsorptive Removal of Herbicides from Water over Nitrogen-doped Carbon Obtained from Ionic Liquid@ ZIF-8. *Chem. Eng. J.* **2017**, *323*, 203−211.
(15) Perez-Aguilar, N. V.; Munoz-Sandoval, E.; Diaz-Flores, P. E.; Rangel-Mendez, J. R. Adsorption of Cadmium and Lead onto Oxidized Nitrogen-doped Multiwall Carbon Nanotubes in Aqueous Solution: Equilibrium and Kinetics. *J. Nanopart. Res.* **2010**, *12*, 467−480.
(16) Shin, K. Y.; Hong, J. Y.; Jang, J. Heavy Metal Ion Adsorption Behavior in Nitrogen-doped Magnetic Carbon Nanoparticles: Isotherms and Kinetic Study. *J. Hazard. Mater.* **2011**, *190*, 36−44.
(17) Modi, A.; Bhaduri, B.; Verma, N. Facile One-step Synthesis of Nitrogen-doped Carbon Nanofibers for The Removal of Potentially Toxic Metals from Water. *Ind. Eng. Chem. Res.* **2015**, *54*, 5172−5178.
(18) Yang, B.; Yu, C.; Yu, Q.; Zhang, X.; Li, Z.; Lei, L. N-doped Carbon Xerogels As Adsorbents for The Removal of Heavy Metal Ions from Aqueous solution. *RSC Adv.* **2015**, *5*, 7182−7191.
(19) Luo, C.; Duan, W.; Yin, X.; Kong, J. Microwave-absorbing Polymer-derived Ceramics from Cobalt-coordinated Poly (dimethylsilylene) Diacetylenes. *J. Phys. Chem. C* **2016**, *120*, 18721−18732.
(20) Luo, C.; Jiao, T.; Tang, Y.; Kong, J. Excellent Electromagnetic Wave Absorption of Iron-Containing SiBCN Ceramics at 1158 K High-Temperature. *Adv. Eng. Mater.* **2018**, No. 1701168.
(21) Song, Y.; He, L.; Zhang, X.; Liu, F.; Tian, N.; Tang, Y.; Kong, J. Highly Efficient Electromagnetic Wave Absorbing Metal-Free and Carbon-Rich Ceramics Derived from Hyperbranched Polycarbosilazanes. *J. Phys. Chem. C* **2017**, *121*, 24774−24785.
(22) Morant, C.; Andrey, J.; Prieto, P.; Mendiola, D.; Sanz, J. M.; Elizalde, E. XPS Characterization of Nitrogen-doped Carbon Nanotubes. *Phys. Status Solidi A* **2006**, *203*, 1069−1075.
(23) Kagenda, C.; Lule, I.; Paulik, C. Nitrogen-doped Carbon Materials for High Performing Lithium Air Batteries. *S. Afr. J. Chem. Eng.* **2018**, *25*, 32−41.
(24) Susi, T.; Pichler, T.; Ayala, P. X-ray Photoelectron Spectroscopy of Graphitic Carbon Nanomaterials Doped with Heteroatoms. *Beilstein J. Nanotechnol.* **2015**, *6*, 177−192.
(25) Arrigo, R.; Hävecker, M.; Wrabetz, S.; Blume, R.; Lerch, M.; McGregor, J.; Schlögl, R.; et al. Tuning the Acid/Base Properties of Nanocarbons by Functionalization via Amination. *J. Am. Chem. Soc.* **2010**, *132*, 9616−9630.
(26) Simoncic, P.; Armbruster, T. Cationic Methylene Blue Incorporated into Zeolite Mordenite-Na:a Single Crystal X-ray Study. *Microporous Mesoporous Mater.* **2005**, *81*, 87−95.
(27) Danish, M.; Hashim, R.; Ibrahim, M. N. M.; Sulaiman, O. Characterization of Physically Activated Acacia Mangium Wood-based Carbon for the Removal of Methyl Orange dye. *BioResources* **2013**, *8*, 4323−4339.
(28) Zhu, Q.; Moggridge, G. D.; D'Agostino, C. Adsorption of Pyridine from Aqueous Solutions by Polymeric Adsorbents MN 200 and MN 500. Part 2: Kinetics and Diffusion Analysis. *Chem. Eng. J.* **2016**, *306*, 1223−1233.
(29) Zhang, Z.; Zhu, W.; Wang, R.; Zhang, L.; Zhu, L.; Zhang, Q. Ionothermal Confined Self-organization for Hierarchical Porous Magnesium Borate Superstructures as Highly Efficient Adsorbents for Dye Removal. *J. Mater. Chem. A* **2014**, *2*, 19167−19179.
(30) Kundu, S.; Chowdhury, I. H.; Naskar, M. K. Synthesis of Hexagonal Shaped Nanoporous Carbon for Efficient Adsorption of Methyl Orange dye. *J. Mol. Liq.* **2017**, *234*, 417−423.
(31) Alqadami, A. A.; Naushad, M.; Alothman, Z. A.; Ghfar, A. A. Novel Metal−Organic Framework (MOF) Based Composite Material for the Sequestration of U(VI) and Th(IV) Metal Ions from Aqueous Environment. *ACS Appl. Mater. Interfaces* **2017**, *9*, 36026−36037.
(32) Fanou, D.; Yao, B.; Siaka, S.; Ado, G. Heavy Metals Removal in Aqueous Solutions by Two Delta-Diketones. *J. Appl. Sci.* **2007**, *7*, 310−313.
(33) Rahman, M. M.; Adil, M.; Yusof, A. M.; Kamaruzzaman, Y. B.; Ansary, R. H. Removal of Heavy Metal Ions with Acid Activated Carbons Derived from Oil Palm and Coconut shells. *Materials* **2014**, *7*, 3634−3650.

DOI: 10.1021/acsomega.8b01252
ACS Omega 2018, 3, 9888−9898